10TH INTERNATIONAL SYMPOSIUM ON PARTICLE IMAGE VELOCIMETRY – PIV13
Delft, The Netherlands, July 1-3, 2013

Application of stereoscopic PIV for hemodynamic studies of life-sized carotid artery models under pulsatile flow condition

Sarah Kefayati[1], David W. Holdsworth[2] and Tamie L. Poepping[1]

[1] Department of Physics & Astronomy, University of Western Ontario, London, Ontario, Canada
skefayat@uwo.ca

[2] Department of Surgery, University of Western Ontario, London, ON, Canada

INTRODUCTION

One of the major causes of ischemic stroke is embolism of thrombi (i.e. blood clots) that are formed at the site of the atherosclerotic plaque in the carotid artery bifurcation. Certain hemodynamic factors, such as flow disturbances, shear stress forces, and recirculation are linked to thrombosis by enhancing and facilitating platelet activation and aggregation [1, 2]. Any alterations of the local flow patterns that can, in turn, induce altered hemodynamic factors can impact the level of thrombotic activity. Previous clinical studies have shown the association of certain geometrical features of the plaque, namely severity of stenosis (i.e. narrowing), plaque eccentricity (symmetry), and plaque ulceration (irregular surface) to the frequency of cerebrovascular events [3, 4].

As a gold-standard experimental technique, particle image velocimetry (PIV) can provide detailed analysis of spatially and temporally evolving flows. This technique has extensively been applied to hemodynamic studies, primarily to investigate the potential of thrombosis in mechanical heart valves. To date, only three PIV studies (excluding echo PIV studies) have been reported in carotid artery models; Bale-Glickman *et al.* [5] applied planar PIV to two patient-specific stenosed carotid artery models, Vetel *et al.* [6] studied flow in a patient-specific model of a healthy carotid artery using stereo PIV, and Buchmann *et al.* [7] studied a healthy carotid artery model and compared results using tomographic and stereoscopic PIV. All studies were conducted assuming steady inlet flow; although they provide a baseline understanding of flow patterns, pulsatile flow conditions strongly impact the flow dynamics, introducing flow instabilities and high temporal gradients.

We have developed a flow-measurement system applying stereoscopic PIV in a family of life-sized carotid artery models, representing a range of disease progression, under physiologically realistic flow conditions in order to characterize stenosed flow features and investigate the impact of the geometrical features of the plaque on downstream flow patterns. A detailed description of the experimental design features and challenges are described, along with sample results. To demonstrate the capability of this system, flow features extracted from a 70% concentrically stenosed model are presented.

EXPERIMENTAL DESIGN

Flow set-up

Optically transparent, life-sized carotid artery phantoms are manufactured using a lost-core casting technique, as previously described [8, 9]. The phantoms were cast in silicone elastomer (Sylgard® 184, Dow Corning Canada, Inc.; refractive index 1.41–1.43). The geometries were based on the *in vivo* study by Smith *et al.* [10] incorporating a common carotid artery (CCA), internal carotid artery (ICA), and external carotid artery (ECA) with inner diameters of 8 mm (CCA inlet), 5.52 mm (ICA outlet), 4.62 mm (ECA outlet), respectively. In addition to the normal (disease-free) model shown in Figure 1, carotid artery models can incorporate diseased features represented by various geometrical plaque parameters, namely stenosis severity, plaque eccentricity (symmetry), and ulceration. The degree of stenosis severity represents the amount of flow obstruction which, based on NASCET criteria [11], can fall within mild (30-49%), moderate (50-69%), and severe (≥ 70%) classification. An atherosclerotic plaque can form concentrically (i.e. expanding into the lumen equally from opposing walls) or eccentrically (with preferential expansion from one side, in this case the non-flow-divider or outer wall). Plaque ulceration, defined as an excavated necrotic core under a ruptured fibrous cap, can form in various shapes and sizes as previously categorized [12].

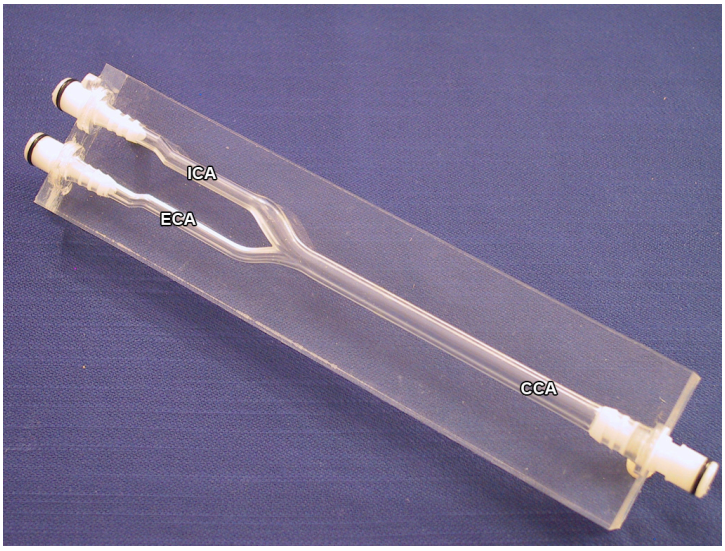

Figure 1 A silicone phantom incorporating a normal (disease-free) geometry of the carotid artery bifurcation.

A computer-controlled pump [13] (CompuFlow 1000, Shelley Medical Imaging Technologies, London, ON, Canada) was used to generate physiologically relevant flow waveforms. The pump generates electrocardiogram (ECG)-simulating signal allowing synchronized acquisition across multiple cardiac cycles. A realistic common carotid flow waveform, based on the *in vivo* waveforms reported by Holdsworth *et al.* [14], was input, and a pair of flow resistors were connected to the ICA and ECA outlets to achieve an approximate flow division of 60:40 (ICA:ECA). Flow waveforms at the inlet of the CCA and outlets of the ICA and ECA were digitally recorded using in-line electromagnetic flow meters (501D, Carolina Medical Electronics, Inc., East Bend NC, USA). The measured waveform (with 10 repeated measures) at the inlet of the CCA had a maximum flow rate of 27.13 (± 0.30) ml s^{-1} at peak systole and a mean flow rate of 6.29 (± 0.09) ml s^{-1} corresponding to Reynolds numbers of 1246 and 289 respectively. Peak and mean flow rates at the outlet of the ECA were measured to be 11.57 (± 0.35) and 2.16 (±0.05) ml s^{-1} respectively, corresponding to Reynolds numbers of 920 and 171. Peak and mean flow rates at the outlet of the ICA were measured to be 12.22 (± 0.19) and 3.56 (± 0.02) ml s^{-1} respectively. Maximum and mean Reynolds numbers calculated based on the narrowest diameter of the ICA stenosis can be estimated to be 1162 and 312 in the 30%-stenosed models, 1627 and 473 in the 50%-stenosed models, and 2712 and 789 in the 70%-stenosed models.

The working fluid was a custom-developed fluid composed of water (47.38% by weight), glycerol (36.94% by weight), and sodium iodide (15.68% by weight) [15]. This blood-mimicking fluid (BMF) has a refractive index of 1.4140 ± 0.0008, matching that of the fabricated silicone phantoms, and an appropriate dynamic viscosity (4.31 ± 0.03 cP) matching that of blood. The fluid was seeded with Rhodamine B-encapsulated microspheres (FLUOSTAR®, EBM Corp., Tokyo, Japan) with mean diameter of 15 μm, excitation peak of 550 nm, and emission peak of 580 nm. The mean diameter of imaged particles was ~ 2.5 pixels, and the particles were distributed with density no less than 100 particles per 32×32 $pixel^2$ region.

Stereoscopic PIV components and arrangements

The stereoscopic PIV system (LaVision Inc., Ipsilanti, MI, USA) was composed of a continuous-wave Nd:YAG (532 nm, 5.5 W) laser, two high-speed CMOS cameras (1024×1024 pixel, 10 bit) each equipped with 60-mm Nikon objective lenses, 550-nm long-pass filters (Bock Optronics Inc., Toronto, ON, Canada), and Scheimpflug adaptors. The cameras were installed above the phantom with opposing viewing angles of 35º relative to the normal. To address the astigmatism aberration, orthogonal viewing was achieved using a transparent silicone prism placed on top of the phantom. The plane of imaging was in planar view (as opposed to cross-sectional) including the three branches of CCA, ICA, and ECA. A precision translational stage (M-EL120, Newport, Corp., Irvine CA, USA) equipped with a dial indicator (Chicago Dial Indicator Co., Inc., Des Plaines, IL) allowed vertical displacement (to within ± 10 μm) of the phantom for multiple-plane measurements throughout the flow volume. For each phantom incorporating a stenosed model, a volumetric flow field was constructed from an ensemble of 15 planar measurements collected from -3.5 to 3.5 mm with 0.5 mm incremental steps. Image acquisition and vector processing were performed using DaVis 7.2 software (LaVision).

Calibration procedure

Calibration was performed using a LaVision standard type-11 calibration plate with 105×105 mm ($W \times L$) dimensions. The calibration target was aligned with the level of the laser sheet, and only one set of calibration parameters was obtained and applied to all the imaged planes (center and off-center planes). This application was made possible through the transitional arrangement in which only the phantom was displaced in the elevation (z) direction. To ensure identical optical properties, the calibration target was placed in a container filled with BMF to a level 12.5 mm above the target surface, corresponding to the same thickness of silicone above the flow channel in the models. An orthogonal-viewing prism was then placed on top of the fluid resting on two side shelves. Figure 2 shows the experimental arrangements and calibration set-up.

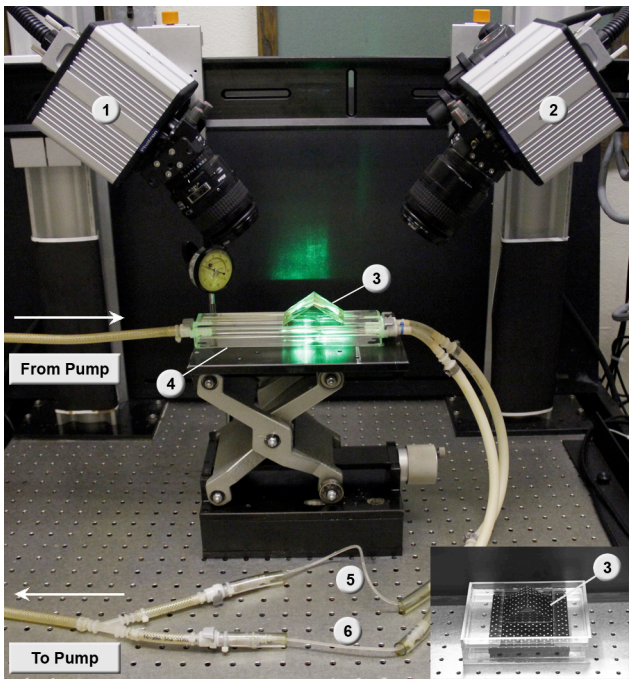

Figure 2 The stereo PIV and flow set-up components: cameras (1, 2), viewing prism (3), block phantom (4), and outlet flow resistors (5, 6). The calibration target set-up is shown in the inset figure in the lower right.

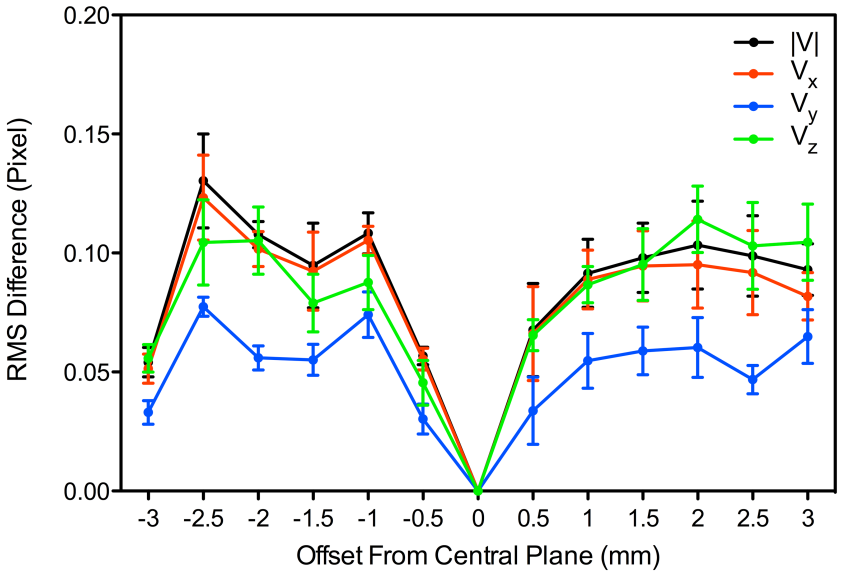

Figure 3 RMS differences between corresponding vectors in maps processed using the central-plane and plane-associated calibration parameters. Error bars represent standard deviation over mean of five repeats.

In adjusting the FOV, it was assured that the calibration plate filled the entire selected FOV. The calibration procedure was carried out in Davis 7.2 software using a 3rd-order polynomial fitting function. After the initial calibration, self-calibration was implemented to account for the possible misalignment of the laser sheet and calibration target. Central-plane images were used to create disparity maps required for self-calibration. The refined calibration parameters were then applied for processing the off-central-plane images. The calibrated images had a scaling factor of ~37 μm/pixel corresponding to the ~ 44 × 40 mm^2 FOV.

To verify the validity of applying central-plane calibration parameters for the off-central planes, a set of volumetric data (covering 13 measurement planes ranging from -3 to +3 mm) was processed twice; each plane was processed once with self-calibration parameters derived from the central-plane images and once again processed with self-calibration parameters obtained using disparity vectors of that plane itself. The two vector maps of each plane were then compared vector by vector, and the difference between the two measurements was calculated as a root mean square (RMS) difference, as shown in Figure 3. Overall, the RMS difference increased for greater vertical offsets; however, the RMS values were within sub-pixel values and less than 0.15 throughout the measurement planes for all three components of velocity. The good agreement between the two measurements can also be verified visually in the side-by-side comparison shown in Figure 4 for a plane of measurement 1.5 mm below the central plane.

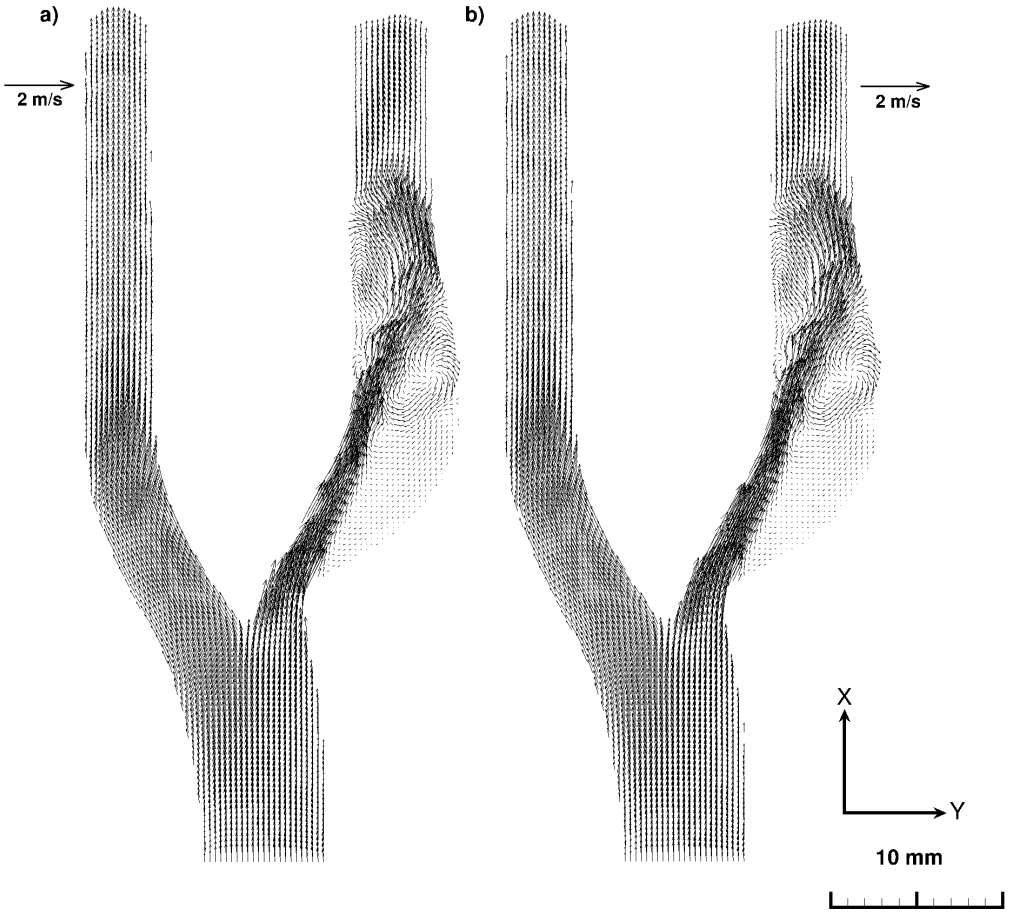

Figure 4 Velocity-vector maps at 1.5 mm below the central plane in a 50% eccentrically stenosed model derived using two different calibration sets: central-plane calibration (a) and plane-associated calibration (b).

Image acquisition and processing

Image acquisition was triggered through the pump synchronization pulse at the start of each waveform cycle. Double-frame images were recorded with time interval settings depending on the measured phantom, ranging from 100 μs for the 70% stenosed model to 400 μs for the normal model. To eliminate the non-flow regions, an algorithmic mask was created individually for each measurement plane based on a RMS image from 100 images and assuming rigid walls. Two-dimensional three-component (2D-3C) velocity fields were generated using the fast-Fourier-transform based cross-correlation algorithm and adaptive multi-pass approach with interrogation window decreasing from 64 × 64 down

to 16 × 16 pixels^2 in the last three passes with 50% overlap throughout. The vector validation was conducted by median filter, and final vector maps were subject to one smoothing pass (3×3 kernel).

Velocity maps were then employed to extract gradient-based features of the flow; for each time point of the cardiac cycle, ensemble-averaged velocity maps from 15 cardiac-cycle velocity sets were used to derive laminar shear stress maps derived using the strain tensor as follows:

$$\tau_{ij} = 2\mu\left(\frac{\partial V_i}{\partial x_j} + \frac{\partial V_j}{\partial x_i}\right),\ i,j = 1,2,3$$

where μ is the dynamic viscosity of BMF, and V_1, V_2, and V_3 correspond respectively to the velocity means (U, V, W) of the instantaneous velocity components u, v, and w in the x, y, and z direction (i.e. x_1, x_2, x_3). Solving the tensor of eigenvalues yields three values out of which the half difference between the maximum and minimum value was used to represent the value of principle shear stress for each vector in the map. The principle shear stress values at the wall boundaries were then used to represent wall shear stress (WSS). For improved visualization of WSS, a smoothed-wall model and processing operations were carried out in the open-source Visualization Toolkit software (VTK, Clifton Park, NY, USA). Shear stress values greater than zero were retained via thresholding. Extraction of the outer polygonal surface produced a coarse wall model. Linear surface subdivision was used to increase triangle vertex density and to aid in smoothing during a volume-preserving geometric smoothing step that followed. Volumetric PIV data were then resampled onto the smoothed wall model producing surface maps of the data for visualization.

Vortex identification was carried out using λ_{ci}-criterion method [16], which yielded 2D swirling-strength maps with directional information of detected vortices. This method is particularly suited for flows with strong shear layers [17].

Evaluation of uncertainty of velocity measurements was carried out using the method introduced by Timmins *et al.* [18], where uncertainty surfaces are created by combination of four major contributing sources of uncertainty, namely particle image size, particle-seeding density, shear rate, and displacement [19]. A set of synthetic images bearing various ranges of the aforementioned four parameters are processed for vector-field estimations using the identical input parameters used to process velocity maps of actual experimental data. The uncertainty is then computed for the distribution of the errors (both bias and random) and is formed into a surface. The next step is to estimate the range of the four parameters for the experimental data followed by applying the previously derived uncertainty surface to estimate the uncertainty value for each vector. The main advantage of this method is estimation of uncertainty associated with each velocity vector. This method was particularly suited for our set of data as regions of high shear rates and large dynamic ranges of velocities are expected. The uncertainties of mean and fluctuating components of velocity (Reynolds shear stress) can also be estimated from the propagation of instantaneous uncertainties as described in the follow-up studies [20, 21]. The mean and fluctuation uncertainties are considered for our study in which a limited sample size (i.e. number of cardiac cycles) is acquired for ensemble-derived parameters such laminar and Reynolds shear stress as well as turbulence intensities. Detailed description of the uncertainty method and the open-source uncertainty codes can be found in [22].

RESULTS AND DISCUSSION

Velocity maps

Figure 5 shows the flow pattern in a 70% concentrically stenosed model. A jet is formed after passing through the stenosis throat and is bounded to the non-flow-divider (i.e. outer) wall. After reattaching and impinging on the outer wall, the jet becomes detached from the wall creating downstream disturbances. Through multiple plane measurements, complex volumetric patterns of the flow, such as helical swirling motion, can be detected. The presence of the helical motion of the flow was also shown previously in flow visualizations of the identical model using digital particle imaging [9]. The vector-map presentation of the cross-sectional view demonstrated the presence of a pair of counter-rotating Dean-type vortices observed above and below the central plane, which continues downstream where flow relaminarizes.

Uncertainty maps

The most challenging model for study was considered the 70% stenosed models in which a wide dynamic range of velocities are expected, varying from ~ 3.5 m/s at peak systole in the jet region to approximately zero in the recirculation zone for the same time point. Also, strong shear layers are present in this model created at the interface of the jet and separated flow. Thus, uncertainty estimations for all time points of the cardiac cycle were considered for a

70% stenosed model to present the maximum expected uncertainty ranges. Figure 6 shows two examples of the uncertainty estimations depicting uncertainty maps associated with the mean of the velocity magnitudes for two time points: peak systole, for which maximum ranges of shear stress are expected, and during the diastolic phase (i.e. cardiac resting). As expected, for both time points, regions of shear layers contribute the greatest to uncertainty with other contributions from downstream velocity fluctuations.

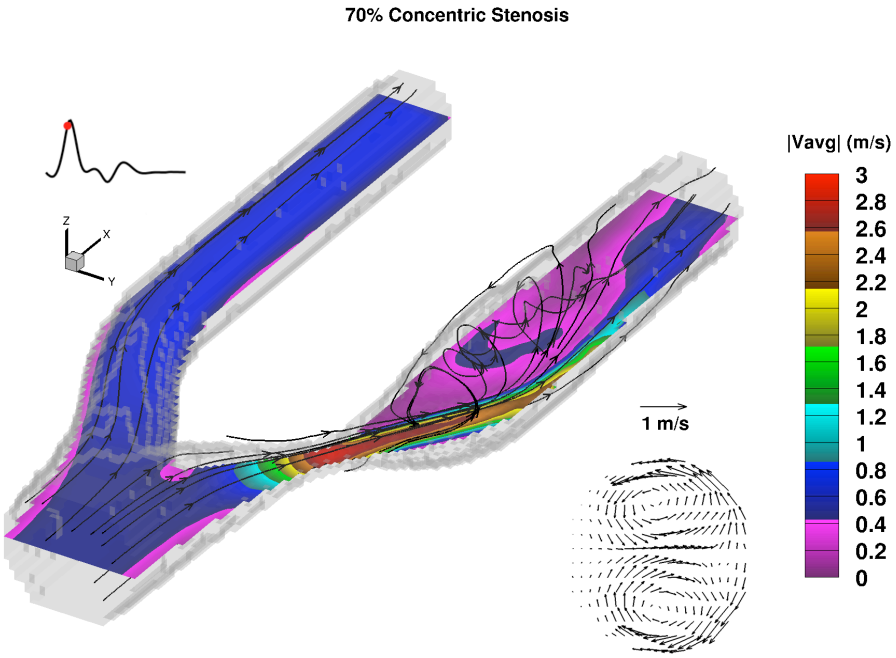

Figure 5 Flow pattern in a 70% concentrically stenosed model for a time point near peak systole. The cross-sectional view was extracted at 17 mm distal to the bifurcation apex.

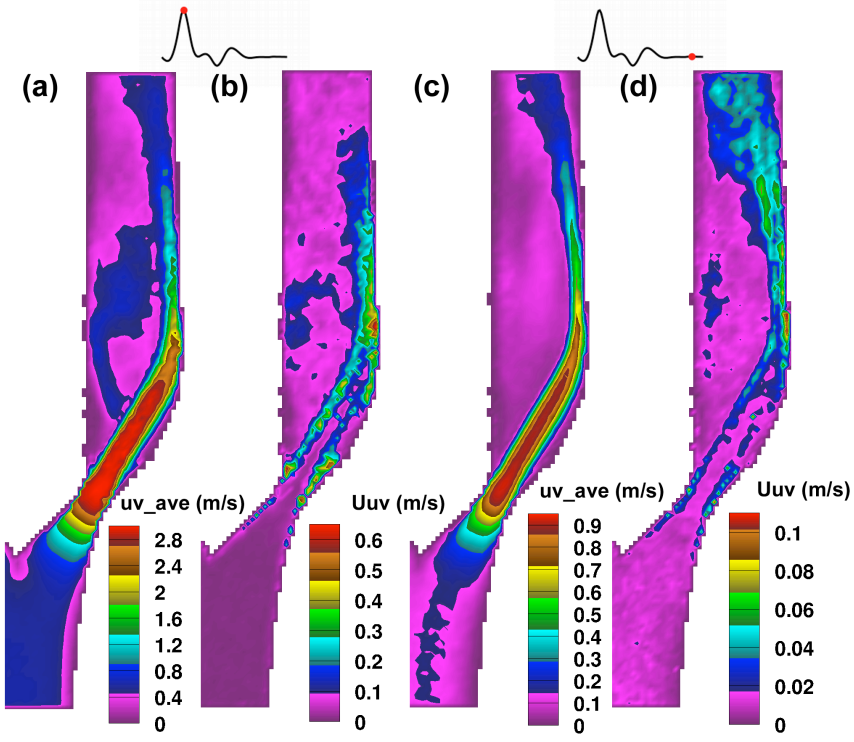

Figure 6 Maps of mean velocity magnitudes (a, c) presented side-by-side to the associated uncertainty maps (b, d) for two time points of the cardiac cycle.

Extraction of thrombosis-related flow features

Thrombosis mechanisms can be facilitated with certain hemodynamic factors that can elevate the level of activation and aggregation. In a particle-path trajectory study, Bluestein *et al.* [23] showed that the platelets, which were initially exposed to high free shear stresses, were entrapped within vortices shedding past the mechanical hear valves. The aggregation of these potentially activated platelets can result in formation of free emboli that can be convected downstream eventually resulting in ischemic stroke. The similar region of vortex shedding was also detected along both sides of the jet passing through the stenosis throat as shown in Figure 7. The vortex shedding starts during the systolic phase of the cardiac cycle, where inviscid instability of shear layers is expected, and persists in the systolic deceleration phase where flow instabilities are prominent.

Pathological levels of WSS can enhance thrombosis activity by damaging the endothelial layer of the plaque, facilitating plaque rupture, or providing suitable environments for platelet activation and aggregation, as previously demonstrated [24, 25]. Depending on the local geometry of the plaque, different patterns of WSS are expected. In the concentric stenoses, elevated WSS regions are located around the stenosis throat, followed by a low-WSS region in the post-stenotic recirculation zone, and a subsequent elevated-WSS region where the jet impinges on the outer wall. Figure 8 shows the patterns of WSS and evolution of the levels during various phases of the cardiac cycle.

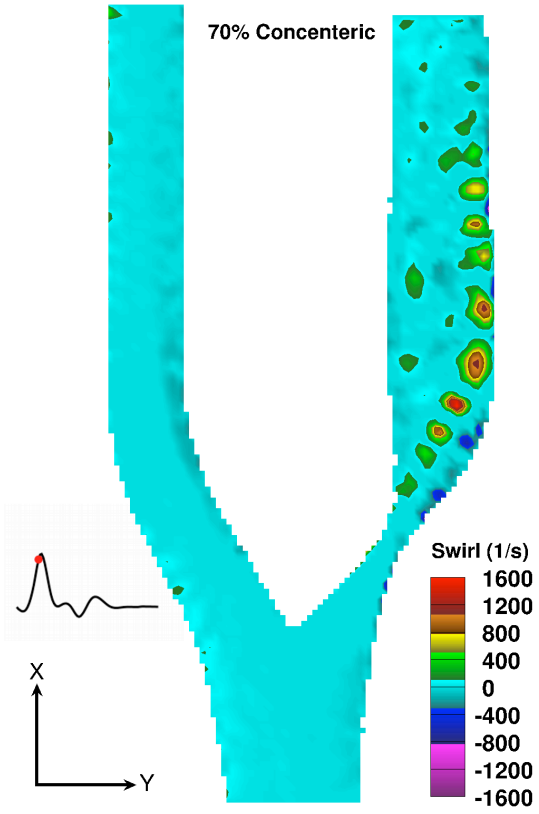

Figure 7 Vortex shedding along shear layers of the jet shown for a time point near peak systole.

In this study, we demonstrated the application of stereoscopic PIV for hemodynamic studies in carotid artery bifurcation phantoms, including severely stenosed models. The high temporal and spatial resolution of PIV allows extraction of gradient-based features of the flow with known association to thrombosis. Exploitation of planar stereoscopic PIV allows volumetric extraction of complex flow features when conducted in multi-plane measurements as demonstrated in the present work. In a comparative study in a carotid artery model, Buchmann *et al.* [7] demonstrated the satisfactory performance of stereoscopic PIV when compared to the more comprehensive tomographic PIV technique.

Possible limitations of the present work include the simplicity of the examined models and the Newtonian blood-mimicking fluid. The idealized models do not include vessel tortuosity and physiological compliance. However, the matched models enable assessment of each individual geometrical variables of the plaque. The use of a Newtonian blood-mimicking fluid is typical given that blood in the larger arteries is typically considered to show Newtonian behavior [26].

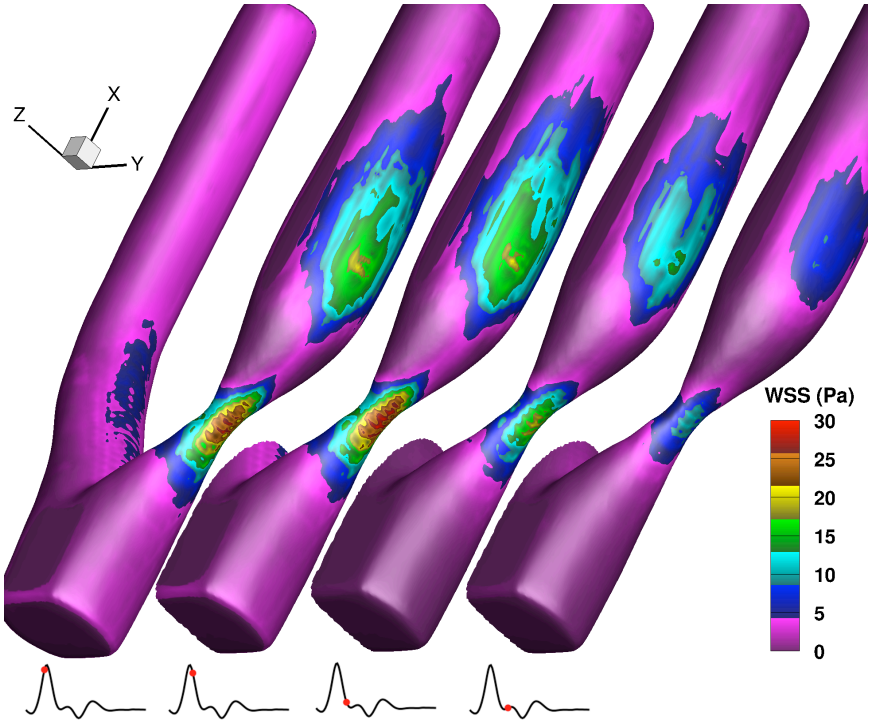

Figure 8 WSS patterns in the ICA branch of a 70% concentrically stenosed model at four different phases of the cardiac cycle.

ACKNOWLEDGEMENTS

The authors would like to acknowledge Hristo Nikolov for the phantom fabrication; Brian Dalrymple and Frank Van Sas for machining and technical help; Scott Warner for assistance with uncertainty codes; Jaques Milner for assistance with VTK; Milad AlemZadeh for assistance with programming. Financial support is acknowledged from the Canada Foundation for Innovation and Ontario Ministry of Research and Innovation (PIV system), Heart and Stroke Foundation of Ontario (operating grant #T-6427), Natural Sciences and Engineering Research Council of Canada (operating grant and UFA salary support of TLP), and Canadian Institutes of Health Research Training Fellowship in Vascular Research (SK).

REFERENCES

[1] Nesbitt WS, Westein E, Tovar-Lopez FJ, et al. "A shear gradient-dependent platelet aggregation mechanism drives thrombus formation" Nature Medicine 15 (2009) pp. 665-U146

[2] Stein PD and Sabbah HN "Hemorheology of turbulence" Biorheology 17 (1980) pp. 301-319

[3] Ohara T, Toyoda K, Otsubo R, et al. "Eccentric stenosis of the carotid artery associated with ipsilateral cerebrovascular events" American Journal of Neuroradiology 29 (2008) pp. 1200-1203

[4] Rothwell PM, Gibson R, and Warlow CP "Interrelation between plaque surface morphology and degree of stenosis on carotid angiograms and the risk of ischemic stroke in patients with symptomatic carotid stenosis" Stroke 31 (2000) pp. 615-621

[5] Bale-Glickman J, Selby K, Saloner D, et al. "Experimental flow studies in exact-replica phantoms of atherosclerotic carotid bifurcations under steady input conditions" Journal of Biomechanical Engineering 125 (2003) pp. 38-48

[6] Vetel J, Garon A, and Pelletier D "Lagrangian coherent structures in the human carotid artery bifurcation" Experiments in Fluids 46 (2009) pp. 1067-1079

[7] Buchmann NA, Atkinson C, Jeremy MC, et al. "Tomographic particle image velocimetry investigation of the flow in a modeled human carotid artery bifurcation" Experiments in Fluids 50 (2011) pp. 1131-1151

[8] Smith RF, Rutt BK, and Holdsworth DW "Anthropomorphic carotid bifurcation phantom for mri applications" Journal of Magnetic Resonace Imaging 10 (1999) pp. 533-44

[9] Poepping TL, Rankin RN, and Holdsworth DW "Flow patterns in carotid bifurcation models using pulsed doppler ultrasound: Effect of concentric vs. Eccentric stenosis on turbulence and recirculation" Ultrasound in Medicine and Biology 36 (2010) pp. 1125-1134

[10] Smith RF, Rutt BK, Fox AJ, et al. "Geometric characterization of stenosed human carotid arteries" Academic Radiololgy 3 (1996) pp. 898-911

[11] North American Symptomatic Carotid Endarterectomy Trial (NASCET) investigators "Clinical alert: Benefit of carotid endarterectomy for patients with high-grade stenosis of the internal carotid artery" Stroke 22 (1991) pp. 816-7

[12] Wong EY, Nikolov HN, Thorne ML, et al. "Clinical doppler ultrasound for the assessment of plaque ulceration in the stenosed carotid bifurcation by detection of distal turbulence intensity: A matched model study" European Radiology 19 (2009) pp. 2739-49

[13] Holdsworth DW, Rickey DW, Drangova M, et al. "Computer-controlled positive displacement pump for physiological flow simulation" Medical & Biological Engineering & Computing 29 (1991) pp. 565-570

[14] Holdsworth DW, Norley CJ, Frayne R, et al. "Characterization of common carotid artery blood-flow waveforms in normal human subjects" Physiological Measurement 20 (1999) pp. 219-40

[15] Yousif MY, Holdsworth DW, and Poepping TL "A blood-mimicking fluid for particle image velocimetry with silicone vascular models" Experiments in Fluids 50 (2011) pp. 769-774

[16] Kefayati S and Poepping TL "Transitional flow analysis in the carotid artery bifurcation by proper orthogonal decomposition and particle image velocimetry" Medical Engineering and Physics 35 (2013) pp. 898-909

[17] Zhou J, Adrian RJ, Balachandar S, et al. "Mechanisms for generating coherent packets of hairpin vortices in channel flow" Journal of Fluid Mechanics 387 (1999) pp. 353-396

[18] Timmins BH, Wilson BW, Smith BL, et al. "A method for automatic estimation of instantaneous local uncertainty in particle image velocimetry measurements" Experiments in Fluids 53 (2012) pp. 1133-1147

[19] Raffel M, Willert CE, Wereley ST, et al. "Particle image velocimetry" Springer (2007)

[20] Wilson BM and Smith BL "Uncertainty on piv mean and fluctuating velocity due to bias and random errors" Measurement Science & Technology 24 (2013)

[21] Wilson BM and Smith BL "Taylor-series and monte-carlo-method uncertainty estimation of the width of a probability distribution based on varying bias and random error" Measurement Science & Technology 24 (2013)

[22] PIV Uncertainty Open-source Codes http://efdl.neng.usu.edu/EFDL/Code.html

[23] Bluestein D, Rambod E, and Gharib M "Vortex shedding as a mechanism for free emboli formation in mechanical heart valves" Journal of Biomechanical Engineering 122 (2000) pp. 125-134

[24] Wootton DM and Ku DN "Fluid mechanics of vascular systems, diseases, and thrombosis" Annual Review of Biomedical Engineering 1 (1999) pp. 299-329

[25] Chiu J-J and Chien S "Effects of disturbed flow on vascular endothelium: Pathophysiological basis and clinical perspectives" Physiological Reviews 91 (2011) pp. 327-387

[26] Pedley TJ "The fluid mechanics of large blood vessels" Cambridge University Press (1980)